An evaluation of discrepancies between CPFE simulations and mean-field approximations for dual phase materials

Shahrzad Mirhosseini[1]* iD, Eisso H. Atzema[1,2] iD, Antonius H. van den Boogaard[1] iD

[1] Chair of Nonlinear Solid Mechanics, University of Twente, 7522 NB Enschede, The Netherlands.

[2] Tata Steel Research and Development, 1970 CA, IJmuiden, The Netherlands.

Abstract

This paper explores the discrepancies observed between 2D and 3D crystal plasticity finite element (CPFE) simulations and mean-field approximations in terms of macroscopic flow curves. Two hypotheses are proposed to address the discrepancies: (1) the type of yield function in the mean-field approach (2) differences in stress states between the two methodologies. Based on the first hypothesis, the type of yield function may influence the stress-strain partitioning in the mean-field approach. Consequently, the von Mises criterion is replaced with the Hershey yield function. To test the second hypothesis, CPFE simulations are extended to 3D to achieve comparable stress states in both methods. This analysis reveals that the exact shape of the yield function has a marginal impact on the discrepancies, whereas the proper 3D stress distribution significantly reduces them. This comprehensive study also uncovers a limitation of the mean-field approach in terms of accuracy in the prediction of macroscopic material response and stress partitioning for a two-phase polycrystalline material.

Keywords: crystal plasticity, finite element simulations, mean-field model, Hershey yield function, arbitrarily-shaped RVEs, periodic boundary conditions

1. Introduction

Accurate prediction of the macroscopic mechanical behavior of polycrystalline materials is a significant challenge in the realm of materials science. These materials, composed of numerous crystallites or grains, exhibit complex interactions under applied mechanical stresses, rendering their mechanical response inherently complicated to predict.

In the context of the computational modeling of polycrystalline materials, full-field methods solve the complete spatial distribution of variables (such as stress or strain) over the entire aggregate, while the mean-field approach simplifies the representation of polycrystalline materials that results in an averaged stress and strain within the aggregate. This is then used as a substitute (uniform) continuum relation. This method has been extensively used due to its computational efficiency. Among the various full-field and mean-field approaches developed so far, the crystal plasticity finite element (CPFE) simulations (full-field-based) and self-consistent (mean-field-based) are widely utilized. Each of these methodologies offers distinct advantages and limitations. The CPFE method is

a full-field approach, as it accounts for the complete spatial distribution of plastic deformation in a material. Self-consistent scheme iteratively updates the material state at each point based on the global behavior of the system.

Pioneering work by Taylor (1938) established the groundwork for these techniques. Hill (1965) introduced a self-consistent approach that extended the theoretical framework for understanding the mechanical behavior of composite materials. Later, developments by Hutchinson (1970) broadened their applicability across various materials and loading conditions. However, simplifying assumptions can lead to inaccuracies, particularly in predicting the macroscopic flow curves of complex materials.

In contrast, CPFE simulations offer a more detailed representation by explicitly modeling the behavior of individual grains and their interactions. Early work by Peirce et al. (1982) demonstrated the potential of CPFE models in capturing the anisotropy and heterogeneity of polycrystalline materials. Later studies by Becker (1991) and Bronkhorst et al. (1992) further validated the superior predictive capabilities of CPFE models for texture evolution and anisotropic hardening behavior. Nevertheless, the higher computational cost of CPFE simulations remains a drawback, especially for large-scale finite element simulations.

A limited number of studies have explored the discrepancies between these two approaches. For instance, Lebensohn & Tomé (1993) compared self-consistent models with finite element approaches, highlighting the limitations of mean-field models in capturing localized deformation patterns. Lebensohn et al. (2004) benchmarked standard and second-order self-consistent models against FFT-based full-field simulations across viscoplastic FCC and HCP polycrystals. They found that for linear behavior, classic self-consistent performs well even with high grain anisotropy; however, in the nonlinear regime, the second-order self-consistent approach more accurately predicts effective properties and stress/strain rate fluctuations closely matching full-field results, while lower-order self-consistent variants fall short. Roters et al. (2011) provided a comprehensive review of CPFEM, outlining its ability to simulate slip, twinning, and transformation mechanisms at the grain scale. They emphasized CPFEM's strength in capturing anisotropic hardening, texture evolution, and localized deformation. The study contrasted CPFEM with mean-field models, showing its superiority in resolving microstructural gradients and heterogeneity. CPFEM was also highlighted as a multiscale tool capable of incorporating dislocation mechanics and experimental calibration. However, its high computa-

tional cost remains a key limitation. Lebensohn et al. (2011) compared full-field methods with homogenization techniques to predict microstructure-property relations in polycrystalline materials. They highlighted that while full-field methods obtain detailed and accurate predictions, mean-field approaches provide computational efficiency. Logé et al. (2012) compared a mean-field grain-category model with a CPFEM model for static and dynamic recrystallization. They showed that while mean-field models are computationally efficient, they fail to capture spatial heterogeneities in stored energy and nucleation, leading to inaccuracies in predicting recrystallized fractions under nonuniform deformation. Further analysis of mean-field and full-field approaches was performed by Segurado et al. (2018), who investigated computational homogenization methods for polycrystals. They compared the predictions of the full-field and mean-field models under various loading conditions and microstructural configurations. Their results demonstrated that while mean-field models offer clear advantages in terms of computational efficiency, they inherently lack the resolution required to capture critical microstructural effects such as grain-scale localization and intergranular stress distributions. Niskanen (2023) compared two types of crystal plasticity models in fatigue modeling: a crystal plasticity finite element model and a self-consistent crystal plasticity model. The study reveals that models yield similar results for a prior austenitic microstructure, while significant differences arise in plasticity and stress distribution with a martensitic microstructure; Their results indicate that finite element models accurately model crack propagation and self-consistent models can only estimate damage.

Due to computational limitations, CPFE simulations are often conducted on 2D microstructures. Self-consistent methods are generally regarded as providing accurate approximations of stress and strain decomposition, so it was anticipated in the study by Mirhosseini et al. (2021) that the average stresses and strains in each phase from CPFE simulations would align closely with those predicted by the self-consistent approach. However, their results indicated discrepancies between the two, which are examined in more detail in this paper.

This article investigates the observed discrepancies of macroscopic flow curves obtained by means of 2D CPFE simulations and the mean-field approach. To elucidate these discrepancies, two hypotheses are proposed. First, the choice of yield function in the mean-field approach may influence the stress-strain partition. In the mean-field model, the von Mises yield criterion is replaced with the Hershey yield function.

Additionally, since the 2D simulations assume a plane strain condition, significant differences arise between the von Mises and Hershey yield functions, particularly with exponents of 6 or 8. The derivatives of the Hershey yield function are obtained analytically to reach asymptotic quadratic convergence in the stress-update algorithm of the computational plasticity solution. This derivation is one of the novelties of the current study.

Second, the difference in stress states between the fully plane strain 2D CPFE simulations and the average plane strain mean-field models is considered as a cause for the discrepancy. To study this hypothesis, CPFE simulations are extended to 3D to harmonize these stress states. Arbitrarily-shaped geometrically-periodic representative volume elements (RVEs) are used in the simulations. It is deduced from the results that changing the yield function type in the mean-field approach has a minor influence on reducing discrepancies. The extension of CPFE simulations to 3D decreases the discrepancy of the austenite phase and two-phase aggregate between 2D CPFE simulations and the mean-field approach. However, this improvement does not hold for the martensite phase, which will be investigated further in this article. The results underline the limitations of the mean-field approach in the prediction of the macroscopic material behavior for high constituent phase contrast.

Plane strain conditions are commonly employed in 2D CPFE simulations of polycrystalline materials to mimic a constrained deformation mode, which partially approximates the out-of-plane constraint that naturally arises in 3D simulations. This choice allows a better approximation of realistic 3D stress states in a 2D framework and is necessary for meaningful comparison between 2D and 3D CPFE results.

2. Methodology and the preceding results

Macroscopic hardening behaviors of a two-phase material composed of soft FCC and hard BCC phases, predicted by 2D CPFE simulations and the mean-field method, are compared in the study of Mirhosseini et al. (2021). In their study, CPFE simulations are conducted on RVEs with hexagonal grains exposed to periodic boundary conditions, while the self-consistent scheme in mean-field evaluates stress and strain partitioning using an averaging over these fields. In the mean-field model, a von Mises yield function is applied to describe the plastic flow in each constituent phase.

2.1. Methodology

In the comparison mentioned earlier in this section, two well-known multiscale modeling approaches are employed, crystal plasticity finite element and mean-field. The fundamental aspects of these two approaches are recapitulated here below.

2.1.1. Crystal plasticity model

Crystal plasticity is an advanced computational tool to model the material's heterogeneities at microscale and micromechanical phenomena. It evaluates the anisotropic behavior of polycrystalline materials exposed to mechanical stresses. These permanent deformations are considered to be mainly driven by dislocation movements. This theory focuses on the crystallographic slip systems, which are defined as the planes and directions along which dislocations glide.

A rate-independent finite strain crystal plasticity model (Asik, 2019; Perdahcıoğlu, 2024) is employed in the current paper to describe the material model at each integration point in finite element simulations in Abaqus/Standard.

In this model, plastic deformation only occurs due to crystallographic slips on each slip system and the influence of plastic deformation caused by twinning and transformation-induced plasticity is ignored. Each slip system α is designated by a unit vector in the slip direction $\mathbf{s}_0^{(\alpha)}$ and a slip plane normal $\mathbf{n}_0^{(\alpha)}$ defined in the reference configuration. It is assumed that the deformation occurs in two steps: an initial plastic deformation from the reference configuration to an intermediate configuration and an elastic deformation and rotation from the intermediate to the final configuration. The total velocity gradient, $\mathbf{L}$ is defined as the summation over the rate of deformation, $\mathbf{D}$ and the spin tensor, $\mathbf{W}$ so that $\mathbf{L} = \mathbf{D} + \mathbf{W}$. It is also decomposed to an elastic and plastic part as:

$$\mathbf{L} = \mathbf{L_e} + \mathbf{L_p} \qquad (1)$$

The plastic component of the total velocity gradient tensor is expressed as the sum of the shear rates $\dot{\gamma}^{(\alpha)}$ across all slip systems, each weighted by the Schmid tensor $\mathbf{P}^{(\alpha)} = \mathbf{s}^{(\alpha)} \otimes \mathbf{n}^{(\alpha)}$:

$$\mathbf{L_p} = \sum_\alpha \dot{\gamma}^{(\alpha)} \mathbf{P}^{(\alpha)} \qquad (2)$$

In this context, $\mathbf{s}^{(\alpha)}$ and $\mathbf{n}^{(\alpha)}$ are determined by considering lattice rotations. Plastic deformation occurs in crystallographic slip when the resolved shear stress $\tau^{(\alpha)} = \sigma : \mathbf{P}^{(\alpha)}$ exceeds the critical slip resistance $\tau_c^{(\alpha)}$. The

corotational rate of the Cauchy stress tensor $\overset{\triangledown}{\sigma}$ is related to the rate of elastic deformation $\mathbf{D_e}$ through the following relationship:

$$\overset{\triangledown}{\sigma} = \mathbb{C}_e : \mathbf{D_e} \tag{3}$$

In Equation (3), $\mathbb{C}_e$ represents the constant elastic stiffness tensor (Sadd, 2009). The current model utilizes a Taylor hardening law. The work hardening law is described by Equation (4).

$$\tau_c^{(\alpha)} = \tau_0 + \mu b \sqrt{\sum_\beta Q^{(\alpha\beta)} \rho^{(\beta)}} \tag{4}$$

in which τ_0 represents the strain-independent lattice friction, μ is the shear modulus, b is the Burgers vector length, $\rho^{(\beta)}$ represents the dislocation density on slip system β, and $Q^{(\alpha\beta)}$ is the interaction matrix that captures the geometrical relationship and positioning of slip systems. This matrix specifies how an increase in dislocation density on slip system β enhances the critical shear strength of slip system α. The diagonal elements of Q reflect self-hardening, while the off-diagonal elements represent the influence of other slip systems.

In the present study, 12 slip systems are adopted for FCC crystals (Hirth & Lothe, 1982). For BCC crystals, 24 slip systems are employed (Asaro, 1983).

The evolution of dislocation densities on slip system α, which primarily depends on the shear rate of this slip system, is described phenomenologically by a linear ordinary differential equation:

$$\dot{\rho}^{(\alpha)} = \frac{\dot{\gamma}^{(\alpha)}}{\gamma^\infty} \left[\rho^\infty - \rho^{(\alpha)} \right] \tag{5}$$

where $\dot{\gamma}^{(\alpha)}$, $\rho^{(\alpha)}$, and $\dot{\rho}^{(\alpha)}$ are the slip rate, dislocation densities, and their rate on the slip system α, respectively. γ^∞ and ρ^∞ denote the reference slip and saturated dislocation densities. Equation (5) describes the equilibrium between dislocation generation via the Frank–Read mechanism and dislocation annihilation. For comprehensive details on the numerical implementation of the stress update algorithm within this model, refer to Asik (2019).

2.1.2. Mean-field approach

The mean-field approach is a powerful model to predict the behavior of polycrystalline materials consisting of numerous grains with diverse orientations and properties. By averaging the effects of individual grains, the mean-field approach simplifies the complex interactions within the material, allowing for rough estimations of macroscopic material response. In the mean-field model, the macroscopic stress $\bar{\sigma}$ and strain rate tensor $\bar{\mathbf{D}}$ are related to the average $\bar{\sigma}_i$ and $\bar{\mathbf{D}}_i$ per phase.

$$\bar{\sigma} = \sum_{i=1}^N f_i \bar{\sigma}_i, \quad \bar{\mathbf{D}} = \sum_{i=1}^N f_i \bar{\mathbf{D}}_i \tag{6}$$

where N is the total number of constituent phases and f_i is the volume fraction of each phase i that sums up to 1 for all phases.

$$\sum_{i=1}^N f_i = 1. \tag{7}$$

The macroscopic relationship between the stress and strain of each individual phase is as follows:

$$\dot{\bar{\sigma}}_i = \mathbb{C}_i^{ep} : \bar{\mathbf{D}}_i. \tag{8}$$

In this context, $\bar{\mathbf{D}}_i$ and $\mathbb{C}_i^{ep}$ represent the average strain rate and elastoplastic tangent in phase i, respectively. The strain concentration tensor, displayed as $\mathbb{A}_i$, takes into account the correlation between the average strain in each individual phase and the overall strain rate $\bar{\mathbf{D}}$.

$$\bar{\mathbf{D}}_i = \mathbb{A}_i : \bar{\mathbf{D}} \tag{9}$$

It has been presumed that the strain in each phase is uniform (Eq. (9)). Using Equations (8) and (9), and the first equation of Equation (6), the homogenized elastoplastic tangent of the compound is obtained as:

$$\mathbb{C}^{ep} = \sum_i f_i \mathbb{C}_i^{ep} : \mathbb{A}_i \tag{10}$$

There are various schemes in the mean-field approach and the Eshelby solution (Eshelby 1957; 1959), forms their foundation. This solution describes the elastic field within an ellipsoidal inclusion embedded in an infinite homogeneous medium and provides the necessary insights into the stress and strain distribution around inclusions. This theoretical framework underpins the equivalent inclusion theory, which approximates the behavior of heterogeneous materials by replacing complex inclusions with simpler, equivalent ones that produce the same overall effect.

An isotropic yield function is used in the mean-field approach. The self-consistent scheme is one of the best-known schemes for its precision. This scheme has been applied in this article. The assumption is that the inclusions are located in a matrix with homogenized properties of the RVE, which remain unknown and makes this scheme nonlinear which has to be solved iteratively.

In the study by Perdahcıoğlu (2008), the strain concentration tensor in the self-consistent scheme is derived as:

$$\mathbb{A}_i = [\mathbb{E} : (\mathbb{C}^{ep-1} : \mathbb{C}_i^{ep} - \mathbb{I}) + \mathbb{I}]^{-1} \tag{11}$$

where $\mathbb{C}^{ep}$ is the elastoplastic tangent of the homogenized material, $\mathbb{C}_i^{ep}$ is the elastoplastic tangent of each phase i and $\mathbb{I}$ is the fourth-order identity tensor.

# 3. Considerations on texture and RVE representativeness

To ensure that the observed discrepancies between the CPFE simulations and the mean-field approach are not driven by texture-induced anisotropy, the RVE in the CPFE simulations is generated using randomly assigned crystallographic orientations in the study of Mirhosseini et al. (2023). Their approach leads to a statistically isotropic texture which was verified through inverse pole figures exhibiting uniform orientation distribution along principal directions (not shown for reasons of brevity). Consequently, the isotropic yield function employed in the mean-field approximation is consistent with the isotropic crystallographic character of the microstructure in the CPFE model. This implies that deviations in macroscopic stress-strain responses between the two methods are not attributed to texture effects.

Although the literature acknowledges that large grain counts on the order of 1000 or more may be necessary to accurately resolve microscale fields such as local deformation or rotation, this requirement does not necessarily apply to macroscopic analyses. Prior work by Mirhosseini et al. (2023) has demonstrated that an RVE consisting of approximately 125 grains is sufficient to accurately capture macroscopic isotropic responses when crystallographic orientations are randomly assigned. Their study includes a convergence analysis on the number of grains with respect to average mechanical response, showing that 125 grains yield statistically converged flow curves for polycrystalline aggregates. The present study focuses on macroscopic quantities, specifically stress-strain responses and average phase behavior, where such a grain count is demonstrably sufficient and computationally efficient.

Furthermore, although local field variables may exhibit sensitivity to grain-scale orientation variations in small-scale RVEs, the macroscopic quantities investigated in this work, such as aggregate stress-strain behavior, are significantly less affected by such variations when statistically isotropic textures are employed. The findings reported in the investigation by Mirhosseini et al. (2023) showed that different instantiations of 125-grain RVEs with randomly assigned orientations exhibit minimal scatter in flow curve predictions, reinforcing the robustness of this RVE size for macroscopic modeling. It can be concluded that, while larger grain counts may be necessary for studies involving microscale localization or texture evolution, the chosen RVE size in the present analysis is appropriate for its intended scope.

4. Key findings

It can be seen in the results of the comparison made between 2D CPFE simulations and the mean-field method by Mirhosseini et al. (2021) that the averaged true stress versus true strain curve in the prescribed loading direction exhibits a quite good agreement between the two multiscale modeling approaches that are employed (see Fig. 1). However, there is a discrepancy for stress components in the lateral directions (Figs. 2 and 3). The details of the prescribed loading condition and the finite element simulations, used in this comparison, will be discussed in further details in Section 4.1.2. Some assumptions are made about the isotropy of the response of the aggregate that is considered for the comparison. This assumption has been clarified in Section 3. Two hypotheses are given to explain the observed discrepancy. The details of these hypotheses are elaborated upon later in Sections 4.1 and 4.2.
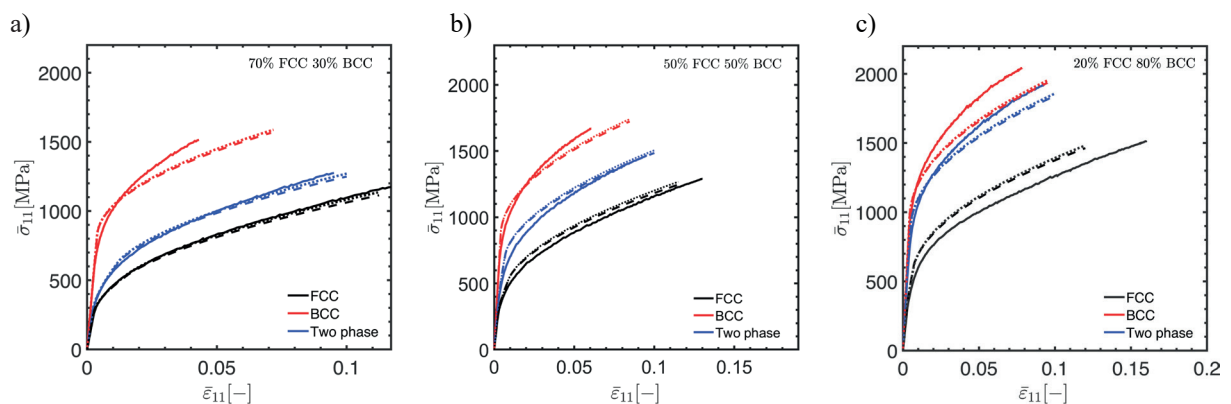
Legend: ▬▬ CPFE simulation, ▪▪▪ Mean-field $J2$ plasticity (Mirhosseini et al., 2021), ⋮⋮⋮ Mean-field Hershey plasticity

Fig. 1. Averaged stress in the loading direction versus the averaged strain in the loading direction for the two-phase material and partitioned in FCC and BCC phases for three cases: a) 70% FCC, 30% BCC; b) 50% FCC, 50% BCC; c) 20% FCC, 80% BCC,
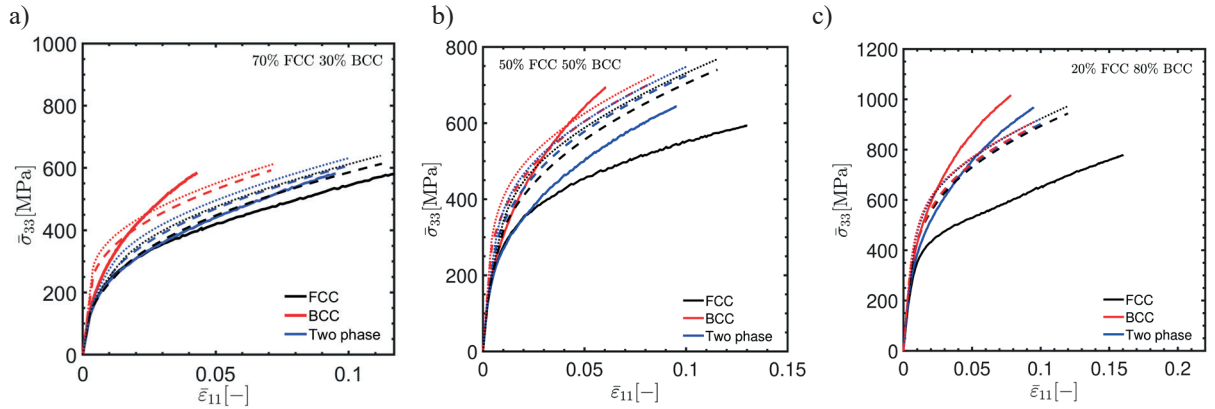
a)

b)

c)
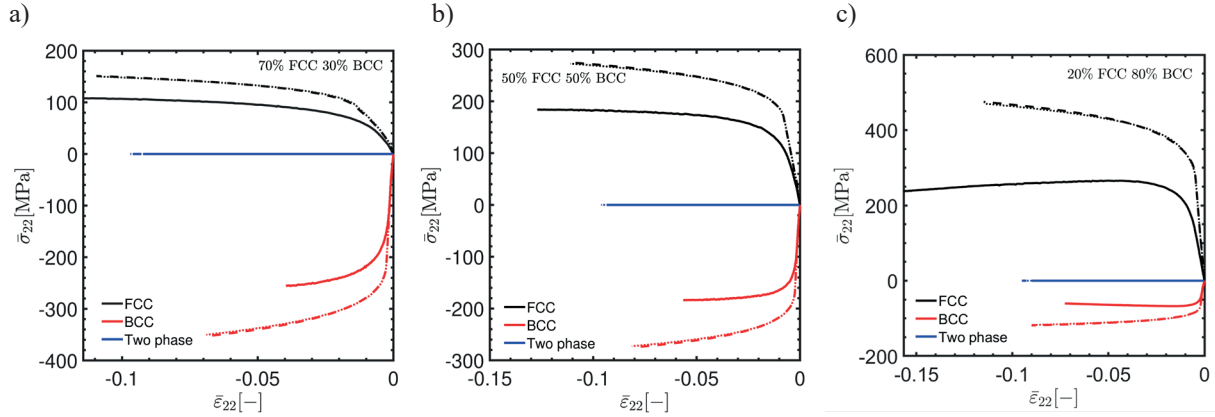
Legend: ▬▬ CPFE simulation, ▬ ▬ ▬ Mean-field *J*2 plasticity (Mirhosseini et al., 2021), ⫶⫶⫶⫶ Mean-field Hershey plasticity

Fig. 2. Averaged stress perpendicular to the loading direction versus the averaged strain perpendicular to the loading direction for the two-phase material and partitioned in FCC and BCC phases for three cases: a) 70% FCC, 30% BCC; b) 50% FCC, 50% BCC; c) 20% FCC, 80% BCC

a)

b)

c)

Legend: ▬▬ CPFE simulation, ▬ ▬ ▬ Mean-field *J*2 plasticity (Mirhosseini et al., 2021), ⫶⫶⫶⫶ Mean-field Hershey plasticity

Fig. 3. Averaged out-of-plane stress in the thickness direction versus the averaged strain in the loading direction for the two-phase material and partitioned in FCC and BCC phases for three cases: a) 70% FCC, 30% BCC; b) 50% FCC, 50% BCC; c) 20% FCC, 80% BCC

4.1. Hypothesis 1:
type of yield function

Based on the first hypothesis, the type of yield function in the mean-field method may affect stress-strain partitioning among phases. In the comparison made by Mirhosseini et al. (2021), the von Mises yield function is utilized to predict the onset of plastic flow in each of the constituent phases. In hypothesis 1, it is postulated that the crystal plasticity simulations for both FCC and BCC phases are better represented by the Hershey yield function (Hershey, 1954). This is in accordance with the investigation by Perdahcıoğlu et al. (2021). Therefore, it is used as an alternative to see if the discrepancies in the lateral stress components are reduced.

4.1.1. Hershey yield function:
implementation

The Hershey yield function is formulated as:

$$\sigma_{eq} = \left(\frac{1}{2} \left| \sigma_2 - \sigma_3 \right|^m + \frac{1}{2} \left| \sigma_3 - \sigma_1 \right|^m + \frac{1}{2} \left| \sigma_1 - \sigma_2 \right|^m \right)^{1/m} \quad (12)$$

in which, σ_{eq} is the equivalent stress, σ_i with $i = 1, 2, 3$ are eigenvalues of the stress tensor and m is a material parameter. Depending on the m value, Hershey yield function approaches other types of yield functions. When $m = 1$ or $m = \infty$, the Hershey criterion equals the Tresca yield function and when $m = 2$, the Hershey criterion equals the von Mises yield function. The values of $m = 8$ and $m = 6$ are usually recommended for met-

als with an FCC or BCC lattice structure, respectively (Hosford, 1996).

The stress update algorithms play a pivotal role in solving computational plasticity problems. A consistent tangent modulus is an essential component in the Newton–Raphson iterative procedure to solve the nonlinear equilibrium equations in finite element analysis. This modulus is applied in the iterative solution procedure to accurately update the stress and strain state.

The first and second derivatives of the yield function are necessary in the derivation of the consistent tangent modulus. The first derivative of the yield function provides the gradient of the yield function. This gradient is essential to determine the direction of the plastic flow. The second derivative ensures the quadratic convergence of the Newton–Raphson method. Without an accurate second derivative, the asymptotic convergence rate may significantly decrease, leading to inefficient and potentially inaccurate solutions. In the Appendices, the first and second derivatives of the Hershey yield function are presented in detail for a full 3D stress state.

A numerical case is considered to make the comparisons. In the mean-field part, a plane strain tensile test with tension in the 11-direction using a prescribed strain in this direction, $\sigma_{22} = 0$ and $\varepsilon_{33} = 0$. In the CPFE part, a 2D plane strain simulation of an exemplary FCC and BCC material, representative of austenite and martensite is carried out. The resulting macroscopic response is fitted by Ludwik's equation for each phase.

4.1.2. Results and discussion

The Hershey yield function is implemented in the mean-field approach to determine when plasticity sets in in each constituent phase. In this section, the same procedure is performed as in Mirhosseini et al. (2021). In Figure 4, a curve fitting to the single-phase FCC and BCC flow curves, obtained from 2D CPFE simulations, is performed to find the macroscopic hardening parameters of the Ludwik type.

The stress state is not purely uniaxial but rather plane strain in this case, and hence the parameters are different from those for the fitted von Mises case in Mirhosseini et al. (2021). The parameters found are listed in Table 1.

Once the single-phase behaviors are known, they are employed in the mean-field model for the homogenization of the two-phase aggregate. Plane strain elements are used in the CPFE simulations meaning that this stress state holds for every single integration point. This renders the CPFE problem a **local plane strain** case. The imposition of plane strain condition in the mean-field approach, however, means an **average plane strain** condition due to the averaged-based nature of the mean-field method. This implies that two different boundary conditions hold in these two methods. The averaged overall stress-strain curves, in parallel to the partitioned stress-strain curves in BCC and FCC phases, are displayed in Figures 1–3. The averaged macroscopic flow curves of the two-phase aggregate, besides the individual FCC and BCC phases obtained by 2D CPFE, mean-field using von Mises yield function (J_2 plasticity) see (Mirhosseini et al., 2021) and mean-field using Hershey yield function, are compared. Based on Figure 1, there is a good to reasonable agreement between the mean-field and 2D CPFE simulation results in the loading direction. This does not hold for the lateral stress components (Figs. 2 and 3). It is also inferred from these figures that using Hershey yield function instead of von Mises hardly influences the results.
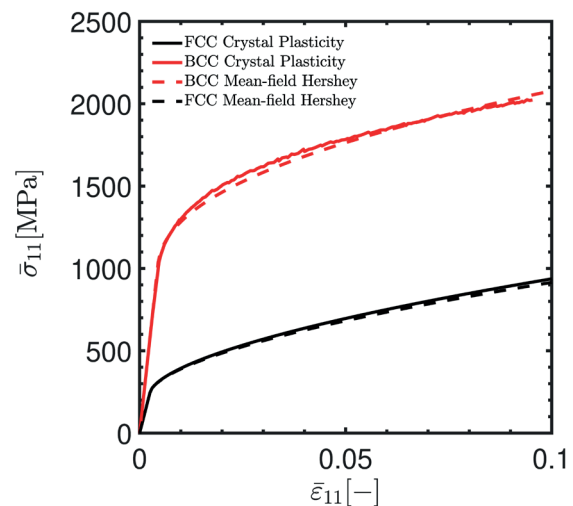

Fig. 4. Fitting macroscopic hardening to the flow curves of the individual FCC and BCC phases, obtained from single-phase 2D CPFE simulations

Table 1. Phase parameters for Ludwik's equation, $\sigma = \sigma_y + k\varepsilon_p^n$

Phase	σ_y [MPa]	k [MPa]	n
FCC	231	2332	0.58
BCC	931	2730	0.45

It is seen in Figure 2 that for both mean-field and 2D CPFE simulations, the averaged macroscopic flow curve for the two-phase material is zero, which means that the **average plane stress** state is accurately represented for both problems.

4.2. Hypothesis 2:
Difference in stress states

In the 2D CPFE simulations of the two-phase material, used in the comparison made by Mirhosseini et al. (2021) and in Section 4.1.2, plane strain elements are used. It is deduced that a **local plane strain-average plane stress** is imposed, meaning that every phase and every grain by itself is in a plane strain state. In the mean-field model, an **average plane strain-average plane stress** state governs the problem. Based on this, it is postulated that different stress states may have caused the discrepancy between mean-field and 2D CPFE simulations evaluations. This postulation will be studied further in this article by 3D CPFE simulations. In the 3D problem, instead of a local plane strain condition, an **average plane strain** condition will be imposed on the problem to approach the stress state in the mean-field model. This is realized by prescribing the average thickness strain in 3D CPFE simulations to zero. It means that the individual grains are allowed to deform in the thickness direction, but the overall elongation in this direction will be zero.

4.2.1. CPFE simulations

To extend the CPFE simulations, a three-dimensional arbitrarily-shaped RVE, as illustrated in Figure 5, is employed.
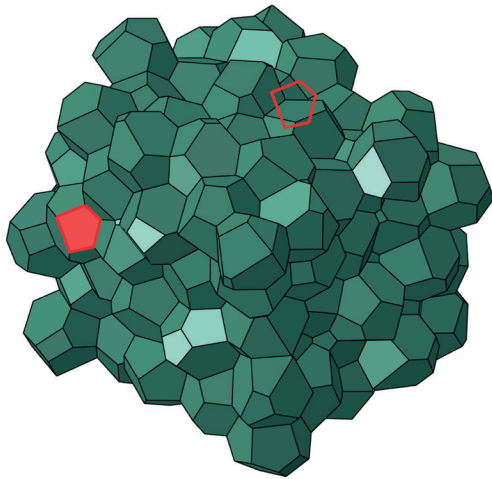

Fig. 5. A geometrically periodic 125-grain 3D RVE with a face couple on the hull highlighted in red

The RVE in Figure 5 is constructed using geometrically periodic Voronoi tessellations generated via Voro++ software (Rycroft, 2009), where Lloyd's algorithm (Lloyd, 1982) is applied over 1000 iterations to ensure a uniform grain size distribution (the periodicity in geometry is illustrated using the two opposite faces highlighted in red in Figure 5). A conforming mesh is generated to facilitate the application of periodic boundary conditions (PBCs), which are imposed by prescribing a macroscopic deformation gradient tensor and constraining the corresponding boundary nodes. Each grain is randomly assigned a phase (austenite or martensite) according to the prescribed volume fractions. In 3D, zero average thickness strain is enforced to simulate a plane strain condition. The details of RVE and mesh generation and assignment of periodic boundary conditions are expressed in the study by Mirhosseini et al. (2023). The selected RVE consists of 125 grains. The methodology for determining the RVE size for single-phase simulations is elaborated upon in Mirhosseini et al. (2023) ensuring that the RVE results do not depend on the selection of lattice orientations. The finite element simulation of the RVE is carried out in Abaqus/Standard using the crystal plasticity-based constitutive behavior, described earlier in this paper, as the material model subroutine.

The simulations are performed for a two-phase austenitic martensitic microstructure, with the crystal plasticity material parameters as specified in Table 2. In the comparisons of 2D CPFE simulations with the mean-field approach results, an arbitrary two-phase material with the phases of FCC and BCC crystalographic structure are used. While, for the 3D CPFE simulations a two-phase material with austenite and martensite phases are used. The properties of the austenite and martensite phase in this comparison belong to an advanced high strength steel generation, called DH800.

4.2.2. Comparative analysis of
3D CPFE simulations and mean-field

The 3D CPFE simulation results are compared with the mean-field model in terms of averaged stress-strain components in lateral and loading directions. In the mean-field model, the hardening of each phase is modeled using a saturation-type equation:

$$\sigma_i = \sigma_{y_i} + b_i \sqrt{1 - \exp\left(-c_i \varepsilon_i\right)} \qquad (13)$$

In Equation (13), ε_i is true strain, σ_{y_i}, b_i and c_i are the yield stress and constants for each constituent phase i, respectively. The corresponding parameters used for the mean-field model are presented in Table 3.

Table 2. Calibrated crystal plasticity parameters for austenite and martensite phases
in the microstructure of TRIP-aided DH800 steel

Property	Symbol	Austenite	Martensite
Young's modulus [GPa]	E	207	207
Poisson's ratio	ν	0.3	0.3
Burgers vector length [m]	b	2.86×10^{-10}	2.48×10^{-10}
Initial dislocation density [m^{-2}]	ρ_0	9.00×10^{10}	1.34×10^{14}
Saturation dislocation density [m^{-2}]	ρ_∞	3.00×10^{15}	7.00×10^{15}
Reference slip	γ_∞	10.0	0.3
Initial CRSS [MPa]	τ_0	246	100
Interaction matrix ($\alpha = \beta$)	$Q_{\alpha\beta}$	1.0	1.0
Interaction matrix ($\alpha \neq \beta$)	$Q_{\alpha\beta}$	1.4	1.4

Table 3. Phase properties and fractions

Phase	E [GPa]	ν [–]	σ_{yi} [MPa]	b_i [MPa]	c_i [–]
Austenite	207	0.3	607	321	6.5
Martensite	207	0.3	958	830	15.0

In the single-phase simulations for both austenite and martensite phases, uniaxial loading conditions are applied to the 3D RVEs.
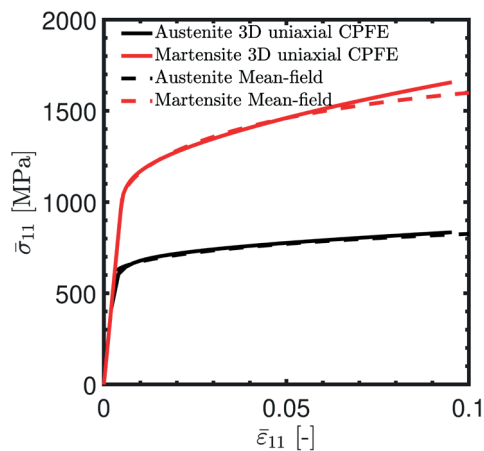

Fig. 6. Comparison of single-phase behaviors obtained by 3D uniaxial CPFE simulations and mean-field for austenite and martensite phases

Figure 6 displays a comparative analysis of the macroscopic flow curves for austenite and martensite, derived from uniaxial 3D CPFE simulations and the mean-field approach. Notably, the discrepancy between the fitted data and the CPFE results for the martensite phase becomes prominent at strains exceeding approximately 6%. However, it is important to consider that such strain levels in martensite are not achieved until a prescribed strain of 10% in the two-phase material, as will be demonstrated later. Consequently, the fitting is deemed sufficiently accurate for this study.

4.2.3. Results and discussion

The comparison is aimed at two different microstructures: 62% austenite and 38% martensite, 83% austenite and 17% martensite.

Case study 1
In this case study, 3D CPFE simulations were conducted on a two-phase material comprising 62% austenite and 38% martensite. These simulations, as in Case study 2, are under **averaged plane strain conditions**. Subsequently, the mean-field model was employed to compute the homogenized behavior of the two-phase material. Figure 7 illustrates the averaged macroscopic flow curves of the two-phase material, along with the stress-strain partitioning in each phase.

The comparison between mean-field and 3D CPFE results for the composite and austenite phases shows a good agreement. However, the martensite phase exhibits significantly softer behavior in the CPFE simulations compared to the mean-field model (see Fig. 7a and c).

A kink is observed in the mean-field $\bar{\sigma}_{33}$ results (see Fig. 7c). This kink in the martensite curve begins at approximately 250 MPa when the austenite phase starts to deform plastically, while the martensite phase remains in the elastic regime.

To verify that the observed behavior is consistent across composites with varying volume fractions of austenite and martensite, the next case study will examine a composite with a different composition.
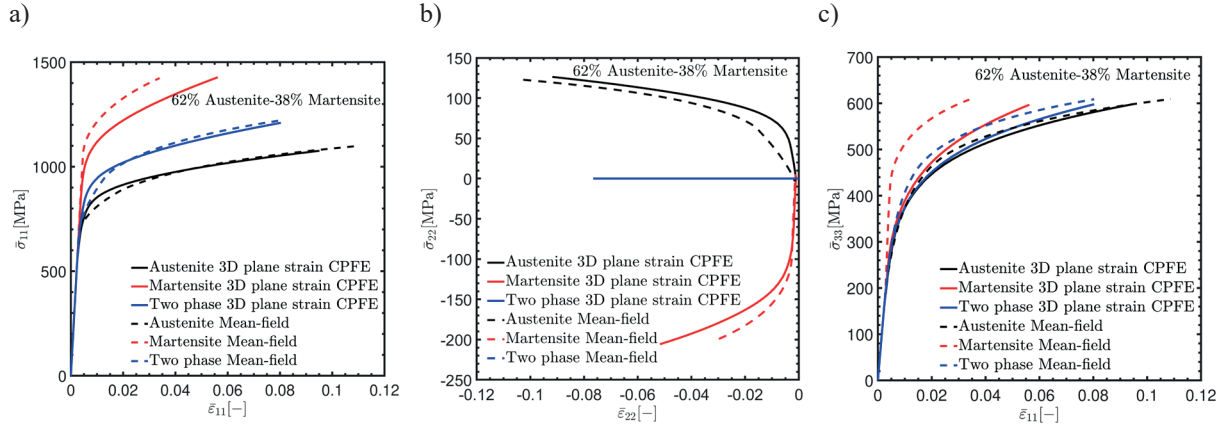
a)
b)
c)

Fig. 7. Averaged flow curves of the two-phase material in addition to stress–strain partitioned in each constituent phase using 3D plane strain CPFE simulations and the mean-field method: a) stress component in the loading direction; b) stress component perpendicular to the loading direction; c) stress component in the plane strain direction

Case study 2

A further investigation was conducted using 3D CPFE simulations on a material composed of 83% austenite and 17% martensite under averaged plane strain conditions. The resulting stress-strain curves were compared with those obtained via the mean-field method, as depicted in Figure 8. The stress-strain curves for the $\bar{\sigma}_{11}$ and $\bar{\sigma}_{33}$ components showed a good agreement for the austenite and two-phase materials, but discrepancies are discernible for the martensite phase. To understand the cause of these discrepancies, the onset of plastification in the austenite and martensite phases was analyzed in the 3D CPFE simulations as strain increased.

The same kink is observed in the mean-field results in Figure 8c at the onset of plastic deformation in austenite. Figure 9 presents histograms of the stress distribution for both phases at various averaged strain levels in the loading direction. At an average strain of 0.0025, all grains remain elastic, resulting in a uniform stress distribution for both phases (see Fig. 9a and b). As the average

strain increases to 0.0030, the stress distribution in the austenite phase becomes non-uniform, indicating the onset of plastic deformation (Fig. 9c). This heterogeneity in the austenite stress distribution also affects the martensite phase, leading to a non-uniform stress distribution (Fig. 9d). With an average strain of 0.004, the heterogeneity in stress distribution further extends.

In both material compositions studied (62% austenite, 38% martensite and 83% austenite, 17% martensite), austenite is the dominant phase by volume fraction. As austenite plastifies, the stress distribution becomes heterogeneous. The mean-field method, however, assumes each phase behaves as a bulk inclusion within a matrix, without considering stress distribution across individual grains. Thus, when plastification begins in the mean-field method, the entire phase yields simultaneously. In contrast, CPFE simulations account for the spatial distribution of grains within the RVE. The CPFE simulations reveal that not all austenite and martensite grains yield and deform plastically at the same time.
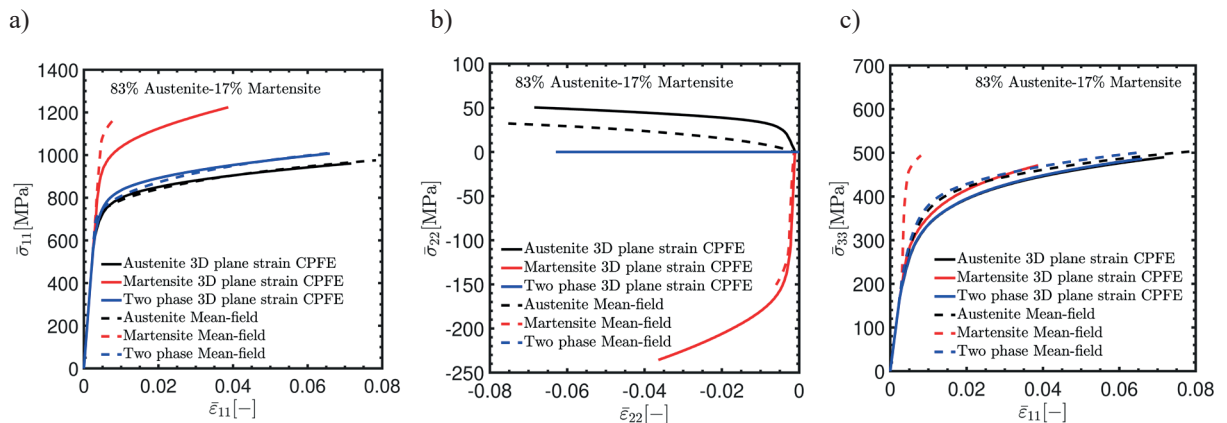
a)
b)
c)

Fig. 8. Averaged flow curves of the two-phase material in addition to stress–strain partitioned in each constituent phase using 3D plane strain CPFE simulations and mean-field method: a) stress component in the loading direction; b) stress component perpendicular to the loading direction; c) stress component in the plane strain direction
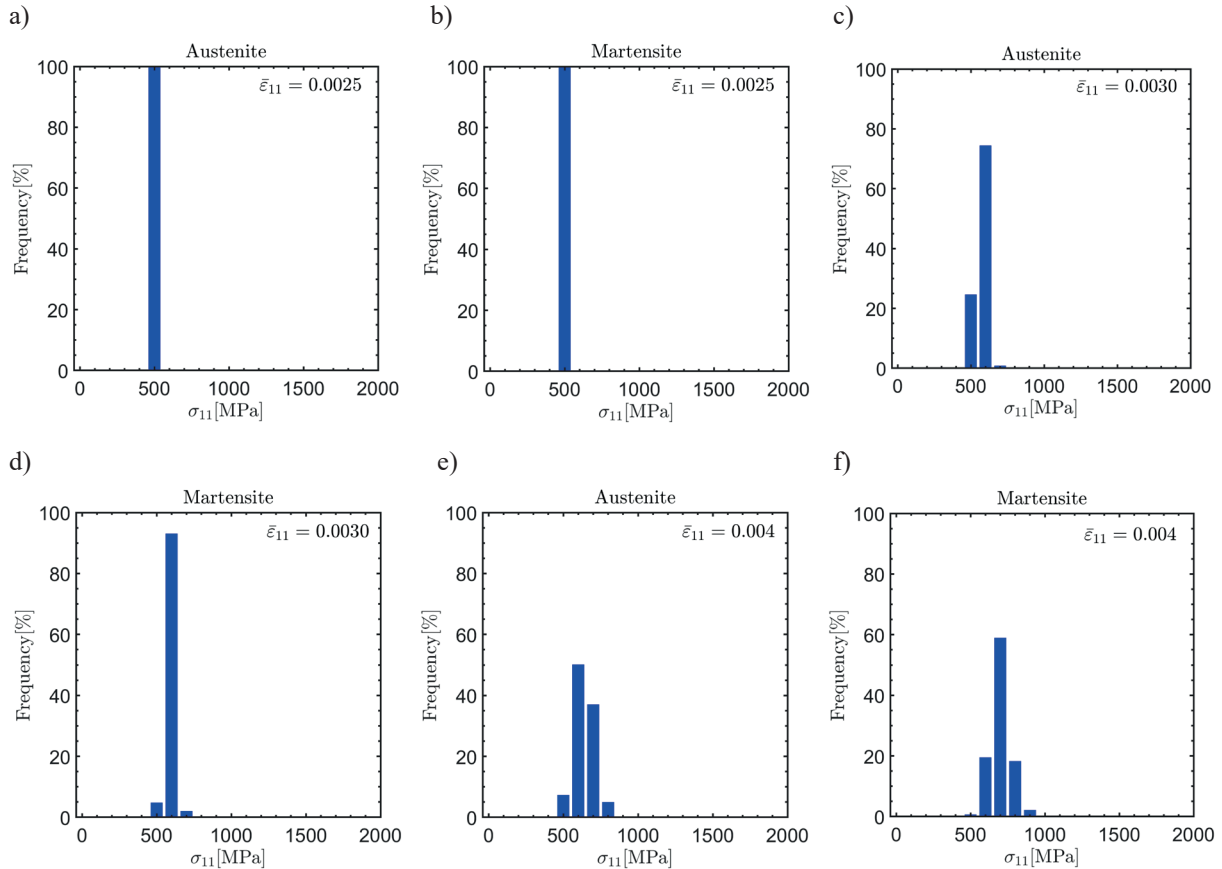
Fig. 9. The percentage of the integration points carrying a specific value of stress for austenite and martensite at the average strain in the loading direction of: a, b) 0.0025; c, d) 0.0030; e, f) 0.0041

This distinction explains the observed discrepancy between the mean-field and 3D CPFE flow curves for martensite. According to Figure 8, the martensite flow curve based on the mean-field model enters the plastic regime abruptly, whereas the 3D CPFE simulations show a more gradual transition. The abrupt plastic deformation of austenite triggers a kink in the martensite, which remains in a fully elastic regime. Although the martensite flow curve does not show an immediate transition into the plastic domain, a change is observed in the elastic portion of the curve when austenite undergoes plastic deformation. This alteration in strain distribution between austenite and martensite causes the stress in the plane strain (33) direction to increase disproportionately with the martensite strain in the tensile (11) direction, assuming the martensite remains fully elastic. As long as martensite is assumed to behave elastically, the predicted average stress in martensite is too high, and the average strain is too low, compared to a full-field simulation that accounts for realistic stress and strain distributions. Martensite grains that yield at relatively early stages significantly soften the average stress-strain curve of the martensite.

Under uniaxial loading, the discrepancy might decrease for the following reasons: The stress state is less complex (one dominant stress component), resulting in less severe stress localization. While stress partitioning between austenite and martensite still occurs, the absence of geometric constraints reduces the build-up of incompatible strains at interfaces. Mean-field models can approximate the average phase response more accurately in such simplified loading paths.

Under equiaxial (hydrostatic) loading, the discrepancy is expected to further reduce for two key reasons: If the applied stress is purely hydrostatic and remains elastic (both austenite and martensite have identical Young's Modulus), both phases might undergo nearly uniform volumetric deformation, minimizing internal stress gradients. Even in elasto-plastic regimes, hydrostatic loading suppresses deviatoric stresses, which are the main driver of incompatibility and localization effects not captured by mean-field models.

However, the validity of these assumptions requires further investigation in future studies. Given the pronounced mechanical contrast between the austenite and martensite phases, particularly in terms of stiffness and load-bearing capacity, the expected homogenized

behavior remains speculative. Moreover, achieving an iso-strain or iso-stress condition (that might occur in equiaxial loading conditions) in CPFE simulations does not inherently imply improved agreement with mean-field predictions. The self-consistent mean-field approach employed in this study represents a compromise between the iso-strain and iso-stress extremes, and does not fully capture the localized phase interactions present in CPFE models.

5. Conclusion

This study provides a detailed analysis of the discrepancies observed between 2D and 3D CPFE simulations and mean-field approach results, focusing on macroscopic flow curves for a two-phase polycrystalline aggregate. The results of this study are summarized here:

- The investigation into the effect of the type of yield function within the mean-field approach, replacing the von Mises criterion with the Hershey yield function, revealed that this alteration has a marginal effect on aligning the results of the two methodologies. The analytical first and second order derivation of the Hershey yield function and its implementation in the stress-update algorithm represent a novel aspect of this work, though its impact on reducing discrepancies was limited.
- The extension of CPFE simulations to 3D was found to significantly reduce the discrepancies, par-

ticularly for the austenite phase and the two-phase aggregate. This extension allowed for comparable stress states between the CPFE and mean-field methods, highlighting the importance of considering dimensionality and stress state differences in predictive modeling. However, this improvement was not observed for the martensite phase.

- This study underscores the limitations of the mean-field approach in accurately predicting macroscopic material responses when dealing with complex, multi-phase polycrystalline materials. The findings suggest that while certain modifications can yield improvements, a potentially more sophisticated modeling technique is necessary to achieve reliable predictions across different material phases. The mean-field model is known as a highly efficient computational method that signifies its application for large-scale simulations and finite element-based industrial applications. One should consider the limitations of this method in order to retain a balance between accuracy and computational efficiency.

Acknowledgements

References

Asaro, R. J. (1983). Crystal plasticity. *Journal of Applied Mechanics*, *50*(4b), 921–934.

Asik, E. E. (2019). *Damage in Dual Phase Steels* [PhD thesis, University of Twente]. University of Twente Research Information. https://doi.org/10.3990/1.9789036548816

Becker, R. (1991). Analysis of texture evolution in channel die compression – I. Effects of grain interaction. *Acta Metallurgica et Materialia*, *39*(6), 1211–1230. https://doi.org/10.1016/0956-7151(91)90209-J

Bronkhorst, C. A., Kalidindi, S. R., & Anand, L. (1992). Polycrystalline plasticity and the evolution of crystallographic texture in FCC metals. *Philosophical Transactions of the Royal Society A: Mathematical, Physical and Engineering Sciences*, *341*(1662), 443–477. https://doi.org/10.1098/rsta.1992.0111

Eshelby, J. D. (1957). The determination of the elastic field of an ellipsoidal inclusion, and related problems. *Proceedings of the Royal Society A: Mathematical, Physical and Engineering Sciences*, *241*(1226), 376–396. https://doi.org/10.1098/rspa.1957.0133

Eshelby, J. D. (1959). The elastic field outside an ellipsoidal inclusion. *Proceedings of the Royal Society A: Mathematical, Physical and Engineering Sciences*, *252*(1271), 561–569. https://doi.org/10.1098/rspa.1959.0173

Hershey, A. V. (1954). The plasticity of an isotropic aggregate of anisotropic face-centered cubic crystals. *Journal of Applied Mechanics*, *21*(3), 241–249. https://doi.org/10.1115/1.4010900

Hill, R. (1965). A self-consistent mechanics of composite materials. *Journal of the Mechanics and Physics of Solids*, *13*(4), 213–222. https://doi.org/10.1016/0022-5096(65)90010-4

Hirth, J. P., & Lothe, J. (1982). *Theory of Dislocations* (2nd ed.). Wiley.

Hosford, W. F. (1996). On the crystallographic basis of yield criteria. *Textures and Microstructures*, *26–27*, 479–493. https://doi.org/10.1155/TSM.26-27.479

Hutchinson, J. W. (1970). Elastic-plastic behaviour of polycrystalline metals and composites. *Proceedings of the Royal Society A: Mathematical, Physical and Engineering Sciences*, *319*(1537), 247–272. https://doi.org/10.1098/rspa.1970.0177

Lebensohn, R. A., & Tomé, C. N. (1993). A self-consistent anisotropic approach for the simulation of plastic deformation and texture development of polycrystals: Application to zirconium alloys. *Acta Metallurgica et Materialia*, *41*(9), 2611–2624. https://doi.org/10.1016/0956-7151(93)90130-K

Lebensohn, R. A., Liu, Y., & Castañeda, P. P. (2004). On the accuracy of the self-consistent approximation for polycrystals: Comparison with full-field numerical simulations. *Acta Materialia*, *52*(18), 5347–5361. https://doi.org/10.1016/j.acta-mat.2004.07.040

Lebensohn, R. A., Castañeda, P. P., Brenner, R., & Castelnau, O. (2011). Full-field vs. homogenization methods to predict micro-structure–property relations for polycrystalline materials. In S. Ghosh, D. Dimiduk (Eds.), *Computational Methods for Microstructure-Property Relationships* (pp. 393–441). Springer New York, NY. https://doi.org/10.1007/978-1-4419-0643-4_11

Lloyd, S. P. (1982). Least squares quantization in PCM. *IEEE Transactions on Information Theory*, *28*(2), 129–137. https://doi.org/10.1109/TIT.1982.1056489

Logé, R. E., Bernard, P., Huang, K., Bag, S., & Bernacki, M. (2012). Mean field and finite element modeling of static and dynamic recrystallization. *Materials Science Forum*, *715–716*, 737–737. https://doi.org/10.4028/www.scientific.net/MSF.715-716.737

Mirhosseini, S., Perdahcıoğlu, E., Atzema, E., & Boogaard, T., van den (2021). On the multiscale analysis of a two phase material: crystal plasticity versus mean field. In A.-M. Habraken (Ed.), *ESAFORM 2021: Proceedings of the 24th International Conference on Material Forming. 14–16 April 2021*.

Mirhosseini, S., Perdahcıoğlu, E. S., Atzema, E. H., & Boogaard, A. H., van den (2023). Response of 2D and 3D crystal plasticity models subjected to plane strain condition. *Mechanics Research Communications*, *128*, 104047. https://doi.org/10.1016/j.mechrescom.2023.104047

Niskanen, I. (2023). *Mean-field crystal plasticity compared to full-field crystal plasticity in fatigue modelling* [Master's thesis, University of Oulu]. OuluREPO. https://urn.fi/URN:NBN:fi:oulu-202306212698

Peirce, D., Asaro, R. J., & Needleman, A. (1982). An analysis of nonuniform and localized deformation in ductile single crystals. *Acta Metallurgica*, *30*(6), 1087–1119. https://doi.org/10.1016/0001-6160(82)90005-0

Perdahcıoğlu, E. S. (2008). *Consitutive Modeling of Metastable Austenitic Stainless Steel* [PhD thesis, University of Twente]. https://doi.org/10.3990/1.9789036527699

Perdahcıoğlu, E. S. (2024). A rate-independent crystal plasticity algorithm based on the interior point method. *Computer Methods in Applied Mechanics and Engineering*, *418*(A), 116533. https://doi.org/10.1016/j.cma.2023.116533

Perdahcıoğlu, E. S., Mirhosseini, S., & Boogaard, A. H., van den (2021). Self-consistent, polycrystal rate-independent crystal plasticity modeling for yield surface determination. In A.-M. Habraken (Ed.), *ESAFORM 2021: Proceedings of the 24th International Conference on Material Forming. 14–16 April 2021*.

Roters, F., Eisenlohr, P., Bieler, T. R., & Raabe, D. (2011). *Crystal Plasticity Finite Element Methods in Materials Science and Engineering*. Wiley.

Rycroft, Ch. H. (2009). *Voro++: A Three-Dimensional Voronoi Cell Library in C++*. https://doi.org/10.2172/946741

Sadd, M. H. (2009). *Elasticity: Theory, Applications, and Numerics*. Academic Press.

Segurado, J., Lebensohn, R. A., & LLorca, J. (2018). Computational homogenization of polycrystals. *Advances in Applied Mechanics*, *51*, 1–114. https://doi.org/10.1016/bs.aams.2018.07.001

Taylor, G. I. (1938). Plastic strain in metals. *Journal of the Institute of Metals*, *62*, 307–324.

Tehrani, J. (2016). *Derivative of eigenvectors of a matrix with respect to its components* [Online forum post]. MathOverflow. https://mathoverflow.net/questions/229425/derivative-of-eigenvectors-of-a-matrix-with-respect-to-its-components

Appendix A

Computation of the first derivative

In Appendix A and B, analytical equations are found for the first and second derivatives of the Hershey yield function by which, in a consistent type of algorithmic tangent, quadratic convergence is ensured. The equations presented in this section are a newly derived closed-form solution for a fully 3D stress state not yet found in the literature. In the derivation of some parts of these equations, algebraic information is utilized from the math forum provided by Tehrani (2016).

To simplify the notations, the yield function in Equation (12), is rewritten as:

$$\left(\frac{1}{2} \left| \sigma_2 - \sigma_3 \right|^m + \frac{1}{2} \left| \sigma_3 - \sigma_1 \right|^m + \frac{1}{2} \left| \sigma_1 - \sigma_2 \right|^m \right)^{1/m} = \qquad \text{(A.1)}$$
$$X^{1/m} = \sigma_{eq}$$

where, X is a scalar used for the sake of simplicity and σ_{eq} is the equivalent stress. The first derivative of the equivalent stress (Eq. A.1) with respect to the stress tensor σ is obtained as:

$$\frac{\partial \sigma_{eq}}{\partial \sigma} = \frac{X^{\frac{1}{m}-1}}{m} \frac{\partial X}{\partial \sigma} \qquad \text{(A.2)}$$

In Equation (A.2), $\partial X / \partial \sigma$ is expressed as:

$$\frac{\partial X}{\partial \sigma} = \sum_{i,j} \frac{m}{2} \left| \sigma_i - \sigma_j \right|^{m-1} \text{sign}(\sigma_i - \sigma_j) \frac{\partial (\sigma_i - \sigma_j)}{\partial \sigma} \qquad \text{(A.3)}$$

where i, j in the subscript of the summation are chosen as elements of $\{23, 31, 12\}$. To complete the derivation of $\partial \sigma_{eq} / \partial \sigma$, based on Equation (A.3), the derivative of principal values (eigenvalues) of the stress tensor with respect to the stress tensor is required. In what follows, this term will be computed. The characteristic equation of the stress tensor is:

$$(\sigma - \sigma_i \mathbf{I}) \cdot e^i = 0 \qquad \text{(A.4)}$$

where σ_i and e^i are the ith eigenvalue and unit eigenvector of the stress tensor, respectively, hence:

$$\sigma = \sum_{i=1}^{3} \sigma_i e^i \otimes e^i \qquad \text{(A.5)}$$

and $\mathbf{I}$ is second-order identity tensor. Variation of Equation (A.4) gives:

$$(d\sigma - d\sigma_i \mathbf{I}) \cdot e^i + (\sigma - \sigma_i \mathbf{I}) \cdot de^i = 0 \qquad \text{(A.6)}$$

Premultiplication of Equation (A.6) with e^i results in:

$$e^i \cdot (d\sigma - d\sigma_i \mathbf{I}) \cdot e^i + e^i \cdot (\sigma - \sigma_i \mathbf{I}) \cdot de^i = 0 \qquad \text{(A.7)}$$

For an arbitrary symmetric second-order tensor called $\mathbf{A}$ and two vectors like $\mathbf{a}$ and $\mathbf{b}$, the following equation holds:

$$(\mathbf{A} \cdot \mathbf{a}) \cdot \mathbf{b} = \mathbf{a} \cdot (\mathbf{A} \cdot \mathbf{b}) \qquad \text{(A.8)}$$

Using the mentioned feature (Eq. (A.8)) of a symmetric tensor like $(\sigma - \sigma_i \mathbf{I})$ and using Equation (A.4), the second term on the left side of Equation (A.7) is zero. It is deduced from the first term (note: $e^i \cdot e^i = 1$):

$$e^i \cdot d\sigma \cdot e^i = d\sigma_i \qquad \text{(A.9)}$$

The term $d\sigma_i$ can be written, using partial derivatives, as:

$$d\sigma_i = \frac{\partial \sigma_i}{\partial \sigma} : d\sigma, \quad \forall d\sigma \qquad \text{(A.10)}$$

Note that for a symmetric second-order tensor like $\mathbf{A}$ and two vectors called $\mathbf{a}$ and $\mathbf{b}$, the following equation holds:

$$\mathbf{a} \cdot \mathbf{A} \cdot \mathbf{b} = \mathbf{A} : \mathbf{a} \otimes \mathbf{b} = \mathbf{a} \otimes \mathbf{b} : \mathbf{A} \qquad \text{(A.11)}$$

Hence, Equation (A.9) can be rewritten as:

$$d\sigma_i = e^i \otimes e^i : d\sigma \qquad \text{(A.12)}$$

Comparing Equation (A.10) and (A.12), the derivative of principal stress values with respect to the stress tensor is found as:

$$\frac{\partial \sigma_i}{\partial \sigma} = e^i \otimes e^i \qquad \text{(A.13)}$$

Hence, Equation (A.3) is simplified as:

$$\frac{\partial X}{\partial \sigma} = \sum_{i,j} \frac{m}{2} \left| \sigma_i - \sigma_j \right|^{m-1} \text{sign}(\sigma_i - \sigma_j) \cdot \qquad \text{(A.14)}$$
$$(e^i \otimes e^i - e^j \otimes e^j)$$

Substituting Equation (A.14) in Equation (A.2), the first derivative of the equivalent stress, based on Hershey yield function, with respect to the stress tensor is obtained.

Appendix B

Computation of the second derivative

The second derivative of the equivalent stress, in Equation (A.1), with respect to the stress tensor is obtained as:

$$\frac{\partial^2 \sigma_{eq}}{\partial \sigma^2} = \frac{X^{\frac{1}{m}-1}}{m} \frac{\partial^2 X}{\partial \sigma^2} + \frac{1}{m}\left(\frac{1}{m}-1\right) X^{\frac{1}{m}-2} \frac{\partial X}{\partial \sigma} \otimes \frac{\partial X}{\partial \sigma} \quad \text{(B.1)}$$

where:

$$\frac{\partial^2 X}{\partial \sigma^2} = \sum_{i,j} \frac{m(m-1)}{2} |\sigma_i - \sigma_j|^{m-2} \, (e^i \otimes e^i -$$

$$e^j \otimes e^j) \otimes (e^i \otimes e^i - e^j \otimes e^j) + \sum_{i,j} \frac{m}{2} |\sigma_i - \sigma_j|^{m-1} \quad \text{(B.2)}$$

$$\text{sign}(\sigma_i - \sigma_j) \times \frac{\partial}{\partial \sigma}(e^i \otimes e^i - e^j \otimes e^j)$$

The following term can be found to simplify the derivative on the second term (right side) of Equation (B.2):

$$d\left(e^i \otimes e^i - e^j \otimes e^j\right) = \frac{\partial}{\partial \sigma}\left(e^i \otimes e^i - e^j \otimes e^j\right) : d\sigma \quad \text{(B.3)}$$

The term on the left side of Equation (B.3) can be written in another way as:

$$d(e^i \otimes e^i - e^j \otimes e^j) = (de^i \otimes e^i + e^i \otimes de^i - de^j \otimes e^j - e^j \otimes de^j) \quad \text{(B.4)}$$

Based on Equation (B.4), the term de^i must be known. In the following part, this term will be assessed. Equation (A.4) can be rewritten as:

$$\sigma \cdot e^i = \sigma_i e^i \quad \text{(B.5)}$$

It is deduced that:

$$d\sigma \cdot e^i + \sigma \cdot de^i = d\sigma_i e^i + \sigma_i de^i \quad \text{(B.6)}$$

It is known that $\|e^i\| = 1$. Hence $de^i \perp e^i$, $\forall i$. Thus due to the symmetry of the stress tensor, the orthogonality proposed earlier and Equation (B.5), the following term is simplified as:

$$(\sigma \cdot de^i) \cdot e^i = de^i \cdot (\sigma \cdot e^i) = \sigma_i(de^i \cdot e^i) = 0 \quad \text{(B.7)}$$

Taking the inner product of Equation (B.6) with e^i, the deduction expressed in Equation (B.7), the unit norm of e^i and the orthogonality of de^i and e^i, it is concluded that:

$$d\sigma_i = (d\sigma \cdot e^i) \cdot e^i \quad \text{(B.8)}$$

Next, taking the inner product of Equation (B.6) with e^k, $k \neq i$, with orthogonality of eigenvectors of a symmetric tensor and due to symmetry of σ:

$$(d\sigma \cdot e^i) \cdot e^k + de^i \cdot (\sigma \cdot e^k) = \sigma_i(de^i \cdot e^k) \quad \text{(B.9)}$$

Using Equation (B.5), Equation (B.9) is rewritten as:

$$(d\sigma \cdot e^i) \cdot e^k + \sigma_k(de^i \cdot e^k) = \sigma_i(de^i \cdot e^k) \quad \text{(B.10)}$$

Equation (B.10) results in:

$$de^i \cdot e^k = \frac{1}{\sigma_i - \sigma_k}(d\sigma \cdot e^i) \cdot e^k \quad \text{(B.11)}$$

The term de^i can be expressed according to its components as:

$$de^i = \sum_{k \neq i}(de^i \cdot e^k)e^k \quad \text{(B.12)}$$

Substitution of Equation (B.11) in Equation (B.12), the following equation is deduced for de^i:

$$de^i = \sum_{k \neq i} \frac{1}{\sigma_i - \sigma_k}(d\sigma \cdot e^i) \cdot e^k \otimes e^k \quad \text{(B.13)}$$

Using Equation (A.11) and substituting Equation (B.13) in Equation (B.4):

$$d(e^i \otimes e^i - e^j \otimes e^j) = [\sum_{k \neq i} \frac{1}{\sigma_i - \sigma_k}(e^k \otimes e^i +$$

$$e^i \otimes e^k) \otimes e^i \otimes e^k - \sum_{k \neq j} \frac{1}{\sigma_j - \sigma_k}(e^k \otimes e^j + \quad \text{(B.14)}$$

$$e^j \otimes e^k) \otimes e^j \otimes e^k] : d\sigma$$

Comparing Equations (B.14) and (B.3):

$$\frac{\partial}{\partial \sigma}(e^i \otimes e^i - e^j \otimes e^j) = \sum_{k \neq i} \frac{1}{\sigma_i - \sigma_k}(e^k \otimes e^i +$$

$$e^i \otimes e^k) \otimes e^i \otimes e^k - \sum_{k \neq j} \frac{1}{\sigma_j - \sigma_k}(e^k \otimes e^j + \quad \text{(B.15)}$$

$$e^j \otimes e^k) \otimes e^j \otimes e^k$$

Substituting Equation (B.15) in Equation (B.2) and the resulting equation in Equation (B.1), the second derivative of equivalent stress with respect to the stress tensor is obtained.